ACS Energy LETTERS

http://pubs.acs.org/journal/aelccp

Capacity Fading Mechanisms in Ni-Rich Single-Crystal NCM Cathodes

Hoon-Hee Ryu,[#] Been Namkoong,[#] Jae-Hyung Kim, Ilias Belharouak, Chong S. Yoon,* and Yang-Kook Sun*

Cite This: *ACS Energy Lett.* 2021, 6, 2726–2734

Read Online

ACCESS | Metrics & More | Article Recommendations | Supporting Information

ABSTRACT: **A series of single-crystal, Ni-rich $Li[Ni_xCo_yMn_{1-x-y}]O_2$ (NCM) cathodes (x = 0.7, 0.8, and 0.9) with particle diameters of ~3 μm are systematically compared with polycrystalline cathodes with corresponding Ni contents. Despite their high resistance to microcracking, the electrochemical performances of single-crystal NCM cathodes, in terms of capacity and cycling stability, are inferior to those of polycrystalline NCM cathodes. In situ XRD and TEM analyses reveal that the lithium concentrations in single-crystal NCM cathodes become spatially inhomogeneous during cycling; this phenomenon is exacerbated by high C rates and Ni contents, resulting in the coexistence of phases with widely different unit cell dimensions within a single cathode particle. This coexistence of two phases induces nonuniform stress that generates structural defects, impairing the diffusion of lithium ions and, eventually, leading to rapid capacity fading.**

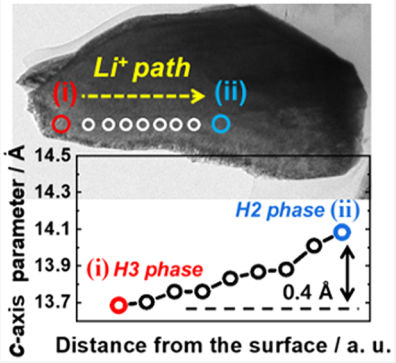

Global efforts to reduce CO_2 emissions have increased the demand for zero-emission electric vehicles (EVs), leading to the rapid growth of the EV market. The market share of EVs is expected to reach 32% of global passenger vehicle sales by 2030,[1] which is made possible by the successful adoption of lithium-ion batteries (LIBs) as their power source. Recent advances in lithium-ion battery (LIB) technology have enabled the realization of EVs that can compete with comparable ICEVs. Nevertheless, there remain several challenges that delay the universal adoption of EVs; the most serious of these challenges are insufficient driving range per charge, short service life, and high cost. These limitations drive the development of high-performance cathode materials for next-generation LIBs because they largely determine the price, energy density, and reliability of LIBs.

Ni-rich layered $[Ni_{1-x-y}Co_x(Mn \text{ and/or } Al)_y]O_2$ (NCM, NCA, and NCMA) cathodes are considered as the main candidates for powering next-generation EVs.[1−3] Increasing the Ni fraction above 90% is the primary approach to increase the energy density, thus enhancing the driving range of associated EVs. However, when a large fraction of Ni is incorporated into these layered cathodes, inherent structural instability caused by the anisotropic lattice contraction in the deeply charged state creates local stress concentrations along the interparticle boundaries.[4,5] The local stress concentrations develop into microcracks along the interparticle boundaries even in the first charged state. Microcracks allow infiltration of electrolyte into the interior of the secondary particle and expose the internal surfaces to the electrolyte attack. The problem is exacerbated by the abundant presence of highly labile Ni^{4+} ions in the deeply charged state. These microcracks undermine the mechanical integrity of the cathode particles in addition to the loss of electrochemical activity from the parasitic reactions at the cathode−electrolyte interfaces. Thus, suppressing the microcracking is a key to alleviating the rapid capacity fading of Ni-rich layered cathodes.

Removing the interparticle boundaries by growing single-crystalline cathode has emerged as a promising strategy.[6−12] Single-crystalline cathodes, free from interparticle microcracking, are shown to improve cycling and thermal stability by minimizing parasitic surface degradation;[6,10] however, single-crystalline cathodes are still in an early stage of development and not sufficiently mature for practical application.[13−15] A large particle size in a single-crystalline cathode increases the Li diffusion length, leading to sluggish kinetics, which is already aggravated by the lack of fast diffusion paths along interparticle boundaries. On the other hand, decreasing the particle size increases the surface-to-volume ratio and the risk of surface degradation. The kinetics of the single-crystal cathode is also largely influenced by

Received: May 27, 2021
Accepted: July 7, 2021
Published: July 13, 2021

https://doi.org/10.1021/acsenergylett.1c01089
ACS Energy Lett. 2021, 6, 2726–2734

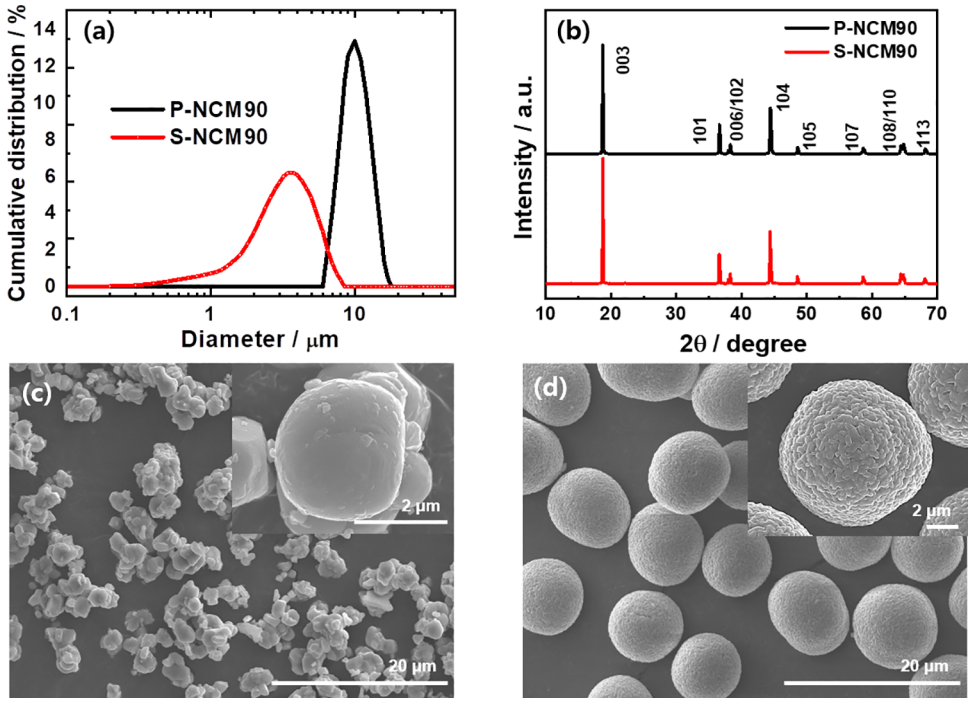

Figure 1. Material characteristics of pristine S-NCM90 and P-NCM90 cathodes: (a) particle size distributions, (b) XRD patterns, and scanning electron microscopy (SEM) images of (c) S-NCM90 and (d) P-NCM90.

morphology and size distribution.[16,17] In addition, most of the single-crystalline cathodes reported to date have focused on materials containing less than 90% Ni because a high Ni fraction requires lowering of the lithiation temperature,[13,14] which makes it difficult to convert a polycrystalline cathode particle to a single-crystal cathode by high-temperature consolidation.

In this study, a comprehensive evaluation of the fundamental properties of single-crystal and polycrystalline cathodes with a wide range of Ni-rich compositions is undertaken. For an accurate comparison, single-crystal NCM cathodes (S-NCM70, S-NCM80, and S-NCM90) and polycrystalline NCM cathodes (P-NCM70, P-NCM80, and P-NCM90) were synthesized with Ni contents of 70, 80, and 90%, respectively. The electrochemical performances of single-crystal and polycrystalline cathodes were correlated with their structural changes to elucidate the dominant capacity fading mechanism of single-crystal cathodes and inform the rational design of advanced cathode materials for LIBs.

Single-crystal and polycrystalline cathodes can be reliably compared provided that their particle size is carefully considered, as it significantly influences the electrochemical performance and physical properties of the cathodes. Based on that single-crystal layered cathodes synthesized tend to range from 1 to 6 μm in previous literature and the particle size of a mass-produced Ni-rich single-crystal cathode by a manufacturer of battery materials is ~3 μm (Figure S1 and Table S1),[6−18] we obtained S-NCM cathodes with a mean particle diameter of ~3.1 μm (D50) from hydroxide precursors synthesized by coprecipitation method (Figure S2). To prepare single-crystal cathodes, the 3 μm sized hydroxide precursor powders were homogeneously mixed with LiOH and calcined for 10 h at 850, 900, and 950 °C for S-NCM90, S-NCM80, and S-NCM70, respectively, under flowing O_2. After calcination, the obtained S-NCM cathodes were finely ground. For realistic comparison, the particle size of polycrystalline cathodes was kept at ~10 μm, which is the industry standard. To obtain P-NCM cathodes, the 10 μm sized hydroxide precursor powders were homogeneously mixed with LiOH and calcined for 10 h at 750, 770, and 810 °C for P-NCM90, P-NCM80, and P-NCM70, respectively, under flowing O_2. The particle size distributions of the cathodes are plotted in Figure 1a and Figure S1. Figure 1a indicates that a P-NCM90 cathode has a narrow particle distribution with a mean particle diameter of 9.71 μm (D50), whereas an S-NCM90 cathode has a relatively wide particle size distribution with a mean particle diameter of 3.08 μm (D50). Due to their small particle sizes, S-NCM cathodes have higher surface areas but lower tap densities than P-NCM cathodes; the surface areas of the S-NCM90 and P-NCM90 cathodes were found to be ~1.46 and ~0.51 $m^2\ g^{-1}$, respectively, and their tap densities were found to be ~2.1 and ~2.5 g cm^{-3}, respectively. The chemical compositions of the synthesized cathode, determined by ICP, are summarized in Table S1. The powder XRD patterns (Figure 1b and Figure S3) reveal that they all have a hexagonal α-$NaFeO_2$-type structure belonging to the $R\bar{3}m$ space group and no detectable impurities. The a-axis and c-axis lattice parameters of the cathodes slightly increase and decrease, respectively, with increasing Ni content (Table S2). The lattice parameters of corresponding single-crystal and polycrystalline cathodes (i.e., with the same chemical composition) are similar and the splitting of the (006)/(012) and (018)/(110) peaks in their XRD patterns indicates that a high degree of crystallinity. The full width at half-maximum (fwhm) values of the (003) peaks in the XRD patterns (listed in Table S2), indicate that line broadening effects are more pronounced in the XRD patterns of the P-NCM cathodes than in those of the S-NCM cathodes, reflecting the different sizes of the single-crystal and polycrystalline cathodes. The morphologies of S-NCM and P-NCM cathode particles are shown in Figures1c,d, and Figure

https://doi.org/10.1021/acsenergylett.1c01089
ACS Energy Lett. 2021, 6, 2726−2734

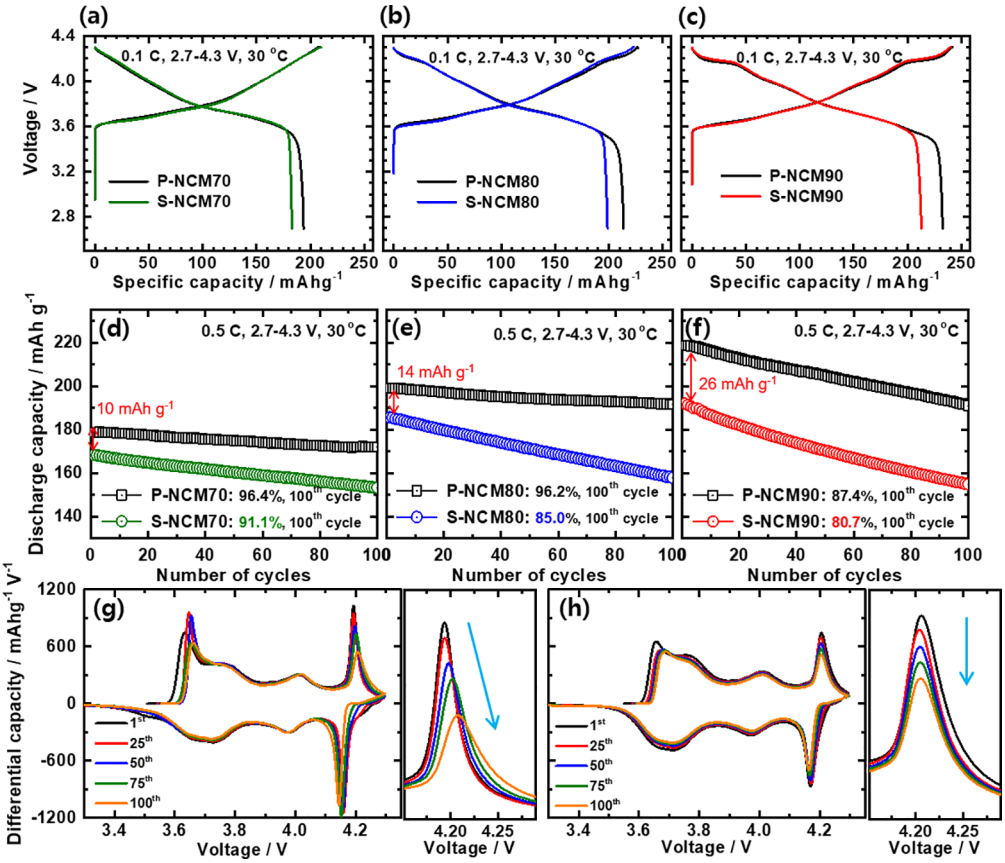

Figure 2. Fundamental electrochemical performances of S-NCM and P-NCM cathodes: (a–c) initial charge–discharge curves at 0.1 C and (d–f) cycling performances at 0.5 C. The differential capacity ($dQ\ dV^{-1}$) curves and magnified redox peaks of the H2–H3 phase transition of cells featuring (g) P-NCM90 and (h) S-NCM90 cathodes.

S4. The S-NCM cathode particles are microsized granules with polygonal shapes; each granule consists of one or several single grains. In contrast, the P-NCM cathode particles consist of nanoscale grains (primary particles) that are densely packed to form nearly spherical secondary particles; these secondary particles show good monodispersity.

Figure 2 summarizes the fundamental electrochemical performances of P- and S-NCM cathodes having 70%, 80%, and 90% of Ni evaluated using 2032 coin-type half cells, cycled between 2.7 and 4.3 V. The characteristic charge–discharge curves in Figure 2a–c show that the capacity of both cathode types increases with increasing Ni content. Although the P-NCM and S-NCM cathodes achieve similar initial charge capacities, the S-NCM cathodes deliver lower discharge capacities than their P-NCM counterparts. The S-NCM cathodes exhibit substantially lower Coulombic efficiencies (CE) compared to the P-NCM counterparts, i.e., 182.8 (CE: 87.2%) and 193.8 mAh g^{-1} (CE: 93.1%) for S-NCM70 and P-NCM70 cathodes, respectively, 199.1 (CE: 89.3%) and 213.5 mAh g^{-1} (CE: 95.3%) for S-NCM80 and P-NCM80 cathodes, respectively, and 212.9 (CE: 88.8%) and 232.6 mAh g^{-1} (CE: 96.4%) for S-NCM90 and P-NCM90 cathodes, respectively. Panels d–f of Figure 2 compare the cycling performances of corresponding S-NCM and P-NCM cathodes. The difference between the initial capacities of the S-NCM and P-NCM cathodes (at 0.5 C) increase with increasing Ni content. The difference was 10 mAh g^{-1} for S-NCM70 and P-NCM70 and 14 mAh g^{-1} for S-NCM80 and P-NCM80 cathodes; however, a significant difference of 26 mAh g^{-1} was observed for the S-NCM90 and P-NCM90 cathodes. The rate capabilities of the P-NCM90 and three S-NCM cathodes were measured to evaluate the difference in their performance (Figure S5a). The capacity of the S-NCM90 cathode decreases faster than that of the P-NCM90 cathode with increasing C rate; at 5 C, the S-NCM90 cathode retains 79.8% of its capacity at 0.1 C, whereas the P-NCM90 cathode retains 90.0%. Although the S-NCM70 and the S-NCM80 cathodes exhibited slightly higher rate capabilities, they were inferior to P-NCM90 cathode. However, the chemical diffusion coefficients of lithium ions in S-NCM cathodes and P-NCM90 cathodes, measured using a galvanostatic intermittent titration technique (GITT), are nearly similar except at the beginning and end of charge (Figure S5b). These results suggest that the poor rate capabilities of the S-NCM cathode are mainly attributed to its morphology; unlike P-NCM cathode particles with networks of grain boundaries offering 3-dimensional fast diffusion paths, Li ions in the S-NCM cathode particles migrate through bulk diffusion mainly through in 2-dimensional pathways along the layer planes, resulting in slow electrochemical reactions.

P-NCM70 and P-NCM80 cathodes retained more than 96% of their respective initial capacities after 100 cycles while the P-NCM90 cathode experienced comparatively significant capacity loss, retaining 87.4% of its initial capacity. In contrast, the cycling stability of the S-NCM cathodes steadily deteriorate with increasing Ni content; the S-NCM70, S-NCM80, and S-NCM90 cathodes retained 91.1, 85.0, and 80.7% of their initial capacities, respectively, after 100 cycles.

https://doi.org/10.1021/acsenergylett.1c01089
ACS Energy Lett. 2021, 6, 2726–2734

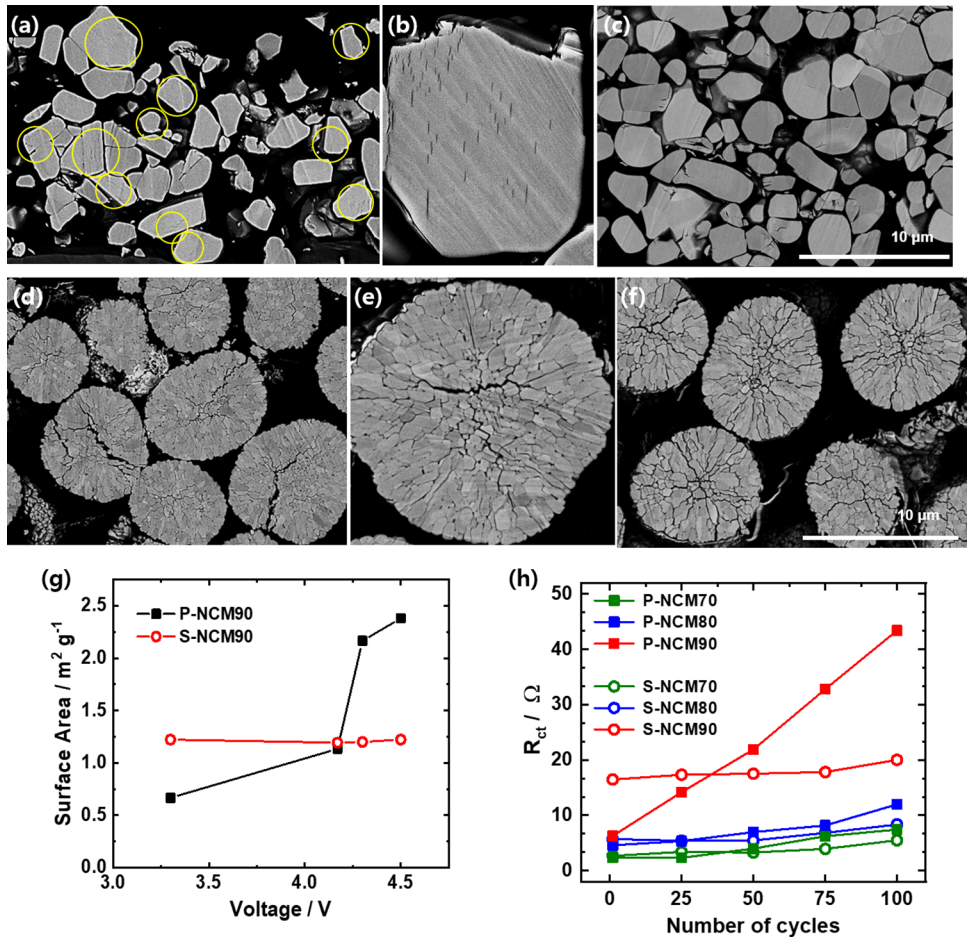

Figure 3. Cross-sectional SEM images of initially charged (to 4.5 V) (a, b) S-NCM90 and (d, e) P-NCM90 cathodes and discharged (c) S-NCM90 and (f) P-NCM90 cathodes after 100 cycles. Particles circled in yellow (a) contain intragranular cracks like the particle shown in (b). (g) The specific surface area of P-NCM90 and S-NCM90 cathodes as a function of the state of charge. (h) Variation in charge transfer resistance (R_{ct}) of S-NCM and P-NCM cathodes during cycling.

The primary degradation mechanism of Ni-rich P-NCM cathodes is well established.[5] In a deeply charged state, H2−H3 phase transitions in Ni-rich layered cathodes cause the abrupt anisotropic contraction/expansion of lattice structures. The resultant structural stress undermined the mechanical stability of the polycrystalline cathode particles because locally accumulated stress was released along grain boundaries by nucleating microcracks. The severity of the anisotropic volume change increased with increasing Ni content; consequently, a cathode with a high Ni content is more prone to developing microcracks that allow the electrolyte to penetrate the cathode particle and attack and damage its internal surfaces. The capacity fading rate of P-NCM cathodes is indirectly revealed by the decaying of the H2−H3 redox peak in their associated differential capacity ($dQ\ dV^{-1}$) curves (Figure 2g and Figure S6). The sharply defined H2−H3 peak in the initial-cycle curve of the P-NCM90 cathode decreases in intensity and becomes increasingly polarized (shifts to a higher voltage) during cycling while the $dQ\ dV^{-1}$ curves of the P-NCM70 and P-NCM80 cathodes hardly change during cycling. It will be shown that extensive microcracking occurs in the P-NCM90 cathode particles due to severe volume changes induced by the H2−H3 phase transitions, and the consequent formation of impedance-increasing surface impurities accelerates capacity fading. In contrast, in the case of the $dQ\ dV^{-1}$ curves of the S-NCM90 cathode, the H2−H3 peak in the initial-cycle curve of the S-NCM90 cathode does not decay as fast as that of the P-NCM90 cathode without any shift in position during cycling despite its inferior cycling stability (Figure 2f). The results suggest that different mechanisms govern the capacity loss of S-NCM and P-NCM cathodes.

Cross sections of charged S-NCM cathodes were examined by SEM to assess their structural damage in deeply charged states. Regardless of the Ni content in the S-NCM cathodes, the incidence of visible microcracks in the low-magnification SEM images of charged S-NCM cathode particles was low (Figure 3a and Figure S7). Although most of the charged (to 4.5 V) S-NCM70 and S-NCM80 cathode particles remained intact, some intragranular cracks were observed in a few S-NCM90 cathode particles, as indicated by yellow circles in Figure 3a. A magnified image of such a charged S-NCM90 cathode particle (Figure 3b) confirms the presence of intragranular cracks. It has been reported that intragranular cracking can occur in single-crystal cathodes when they are overcharged or after long-term cycling.[10,13,19] The intragranular cracking in S-NCM cathode particles mainly stems from the inhomogeneous structural stress induced by lithium concentration differences within the particle. The localized tensile/compressive and shear stresses were released by triggering the gliding of layer planes to nucleate cracks within the single crystal.[13,20] Since the amount of lithium extracted from S-NCM cathodes increases with increasing Ni content,

https://doi.org/10.1021/acsenergylett.1c01089
ACS Energy Lett. 2021, 6, 2726−2734

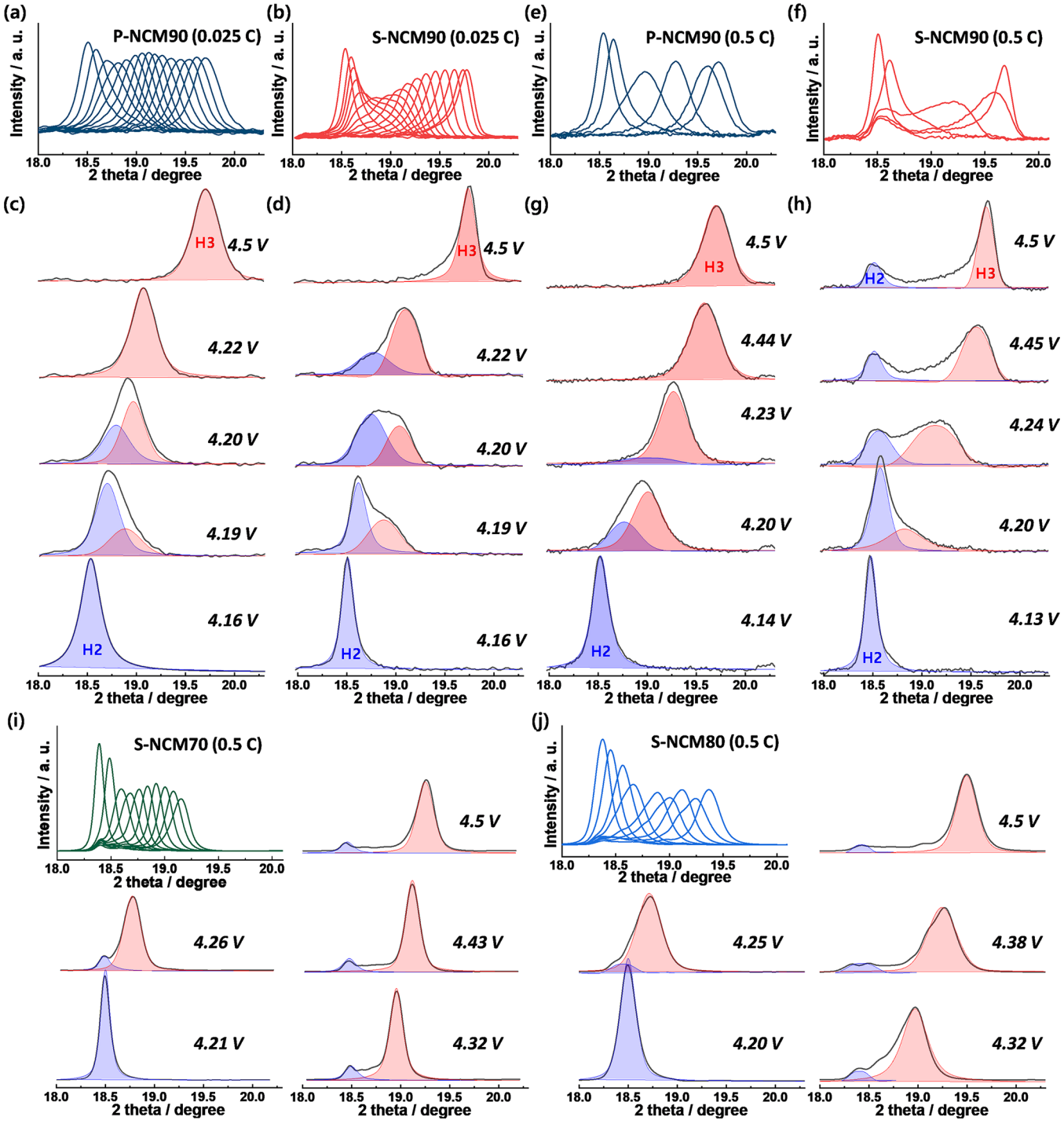

Figure 4. Overlays and deconvolutions of the (003) reflections peaks recorded by in situ XRD during in the voltage range of 4.15−4.5 V: (a,c) P-NCM90 at 0.025 C and (e,g) at 0.5 C, (b,d) S-NCM90 at 0.025 C and (f,h) at 0.5 C, (i) S-NCM70 at 0.5 C, and (j) S-NCM80 at 0.5 C.

the degree of intragranular cracking increases with increasing intensity of the H2−H3 peaks in the associated dQ dV^{-1} curves (Figures S6 and S7). During discharging, the nucleated microcracks close as the structural stresses reverse.[13] After 100 cycles, although some cracks are visible, most of the discharged S-NCM90 cathode particles appear nearly undamaged, maintaining their original shape despite repeated crack nucleation and closure (Figure 3c). In contrast, intergranular cracks are observed in nearly all the charged (to 4.5 V) P-NCM90 cathode particles (Figure 3d). A clear network of microcracks traces the grain boundaries of the secondary particles, isolating adjacent primary particles (Figure 3e). Unlike the S-NCM90 cathode particles, repeated nucleation during long-term cycling (100 cycles) undermines the mechanical stability of P-NCM90 particles to produce microcracks that persist within the secondary particle even in its fully discharged state (Figure 3f). The most critical difference between the intragranular and intergranular cracking behaviors of the S-NCM90 and P-NCM90 cathode particles, respectively, is that the latter exposes the particle interior to

https://doi.org/10.1021/acsenergylett.1c01089
ACS Energy Lett. 2021, 6, 2726−2734

electrolyte attack. As shown in Figure 3g, the exposed area of a P-NCM90 cathode increased gradually with increasing state of charge up to 4.17 V, the voltage at which microcracks start to form, before increasing sharply between 4.17 and 4.3 V, due to the H2−H3 phase transition; the surface area of the P-NCM90 cathode increases from 0.72 to 1.04 (4.17 V), 2.16 (4.3 V), and 2.38 $m^2 g^{-1}$ (4.5 V) with increasing state of charge. In contrast, although the surface area of an S-NCM90 cathode was initially higher than that of a P-NCM90 cathode owing to its small particle size, its surface area hardly changed when charged to 4.5 V. Because of their different cracking behaviors, the variation in the charge-transfer resistance (R_{ct}) of S-NCM and P-NCM cathodes differed appreciably (Figure 3h). The intergranular cracking of the P-NCM90 cathode particles allowed electrolyte infiltration along grain boundaries; the accumulation of an impurity layer associated with the resulting surface degradation as evidenced by the increase in R_{ct} during long-term cycling. As shown in Figure S8, sharply defined fractures and microcracks were formed in charged P-NCM90 cathode particles after 100 cycles whereas P-NCM70 and P-NCM80 cathode particles retained their original spherical morphologies moderately well without clear fracturing. As expected from their R_{ct} results, the original morphologies of S-NCM cathodes were well preserved after 100 cycles, even in their fully charged states; however, the incidence of fine fractures increased with increasing Ni content (Figure S8). The increasing R_{ct} of the P-NCM90 cathode was responsible for the decreasing intensity and increasing polarization of the H2−H3 peaks in the $dQ\ dV^{-1}$ curves of the associated cell during cycling (Figure 2g). In contrast, the R_{ct} of the S-NCM90 cathode hardly changed during cycling, consistent with its relatively unchanging surface area, leading to a slow decaying of the H2−H3 peaks without polarization (Figure 2h).

The aforementioned examinations of the impedance and differential capacity of cells in terms of cathode particle cracking behavior revealed that the capacity fading mechanism of P-NCM cathodes did not apply to S-NCM cathodes. Despite their low R_{ct}, single-crystal cathodes exhibited relatively poor cycling stability. To explicitly monitor the structural changes of the P- and S-NCM90 cathodes during charging, in situ XRD measurements of P-NCM90 and S-NCM90 cathodes were carried out during charge at a low current density of 4.5 mA g^{-1} (corresponding to 0.025 C). Figure S9 shows contour plots of the XRD patterns and the calculated lattice parameters as a function of extracted lithium. During charging, the *a*-axis lattice parameter decreased monotonically while the *c*-axis lattice parameter initially increased and then rapidly decreased with the onset of the H2−H3 phase transition near 4.15 V or $x = 0.7$ in $Li_{1-x}TMO_2$ (TM = transition metal). The P- and S- NCM90 cathodes experienced almost identical intrinsic lattice contraction. The maximum changes in *a*- and *c*-axis lattice parameters were approximately −2.1% and −6.5% up to 4.5 V, respectively. Despite experiencing similar dimensional variations of the respective unit cells, the phase evolution during the H2−H3 phase transition above 4.15 V in the P-NCM90 and S-NCM90 cathodes differs notably. Panels a and b of Figure 4 present two series of overlaid (003) reflections showing the phase evolution in the P-NCM90 and S-NCM90 cathodes between 4.15 and 4.5 V. The (003) reflections of the P-NCM90 cathode shifted smoothly to a higher angle with limited variation in intensity and width. In contrast, the intensity of the (003) peaks for the S-NCM90 cathode decreased considerably and the peaks became asymmetric due to the presence of multiple phases at ∼4.2 V, corresponding to the H2−H3 phase transition. Beyond 4.2 V, the (003) reflections partially recovered their intensity and shape with increasing voltage until 4.5 V. The considerable variations in intensity and symmetry during the phase transition imply nonuniform strain caused by distortions in structure.[5,21] To better trace differences in the phase evolution of P- and S-NCM90 cathodes, the (003) reflections were detailedly compared by assuming that a single-phase or a mixture of two phases exist. The deconvoluted (003) reflections are shown in Figure 4c,d. The deconvoluted peaks for the P-NCM90 cathode in Figure 4c show that two phases coexisted up to 4.2 V, corresponding to the voltage of the apex of the H2−H3 peak in the associated $dQ\ dV^{-1}$ curve. In the case of the S-NCM90 cathode, the coexistence of two phases was observed at 4.19 V and persisted even above ∼4.3 V at which the H2−H3 transition should be complete and only single should exist based on the $dQ\ dV^{-1}$ curve. The in situ XRD data of the S-NCM90 cathode suggests sluggish kinetics for the H2−H3 phase transition that could generate a nonuniform distribution of lithium within the cathode. The structural distortion was more pronounced at a high C rate. Figure 4e−h show the evolution of the (003) reflection peaks of the cathodes recorded during charge at a higher current density of 90 mA g^{-1} (corresponding to 0.5 C). Despite the high C rate, the (003) reflections for the P-NCM90 cathode retained their nearly symmetrical shape above 4.14 V, reflecting that the H2 phase is rather abruptly converted to the H3 phase (Figure 4e,g). For the S-NCM90 cathode, in contrast, the sluggish phase transition resulted in a clearly visible residual H2 phase even at 4.5 V (Figure 4f,h). In addition, unlike the P-NCM90 cathode, the H2 phase in the S-NCM90 cathode did not shift during charging such that two clearly separated peaks were observed above 4.3 V. At 4.5 V, the two deconvoluted peaks were approximately 1° apart, and a residual area remained beneath the curve between the two peaks. The clear separation between the deconvoluted (003) peaks indicates inhomogeneity in lithium concentration and consequent nonuniform strain within the S-NCM90 cathode. Despite the nonuniform strain, the (003) reflection peak of the S-NCM90 cathode nearly recovered to its initial state during discharge, indicating the reversibility of the H2−H3 phase transition (Figure S9). To further investigate whether S-NCM cathodes with low Ni also experience the sluggish kinetic reaction at high current density, we performed in situ XRD measurements. The (003) reflection peaks of the S-NCM70 cathode maintained their symmetrical shape without severe broadening up to a fully charged state of 4.5 V at a specific current density of 0.025 C (Figure S10) and 0.2 C (Figure S11). However, during the charge at a higher C rate of 0.5 C (Figure 4i, Figure S11, and S12), the peaks of the S-NCM70 cathode broadened and decreased in intensity between 4.15 and 4.5 V, remaining a residual peak at 18.4°. Similarly, the (003) reflection peaks of the S-NCM80 cathode broadened much asymmetrically when charged at 0.5 C than 0.2 C (Figure 4j and Figure S12). However, unlike S-NCM cathodes, the (003) peaks of P-NCM70 and P-NCM90 cathodes shifted smoothly to a higher angle without severe broadening during even 1 C charging (Figures S11 and S13). These results suggest that single-crystal cathodes experience more severe structural inhomogeneity at high C rates, likely attributable to their long diffusion paths, and the extent of structural

https://doi.org/10.1021/acsenergylett.1c01089
ACS Energy Lett. 2021, 6, 2726−2734

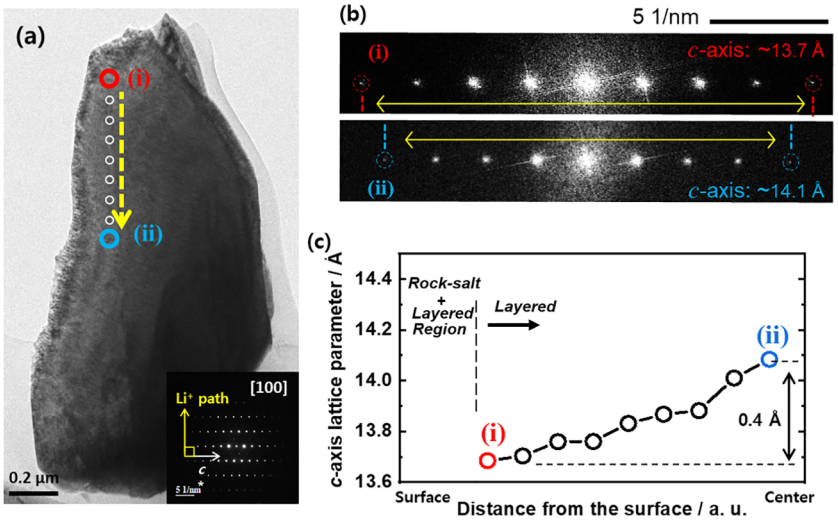

Figure 5. (a) TEM image of the S-NCM90 cathode particle charged to 4.3 V at 0.5 C and (b) part of electron diffraction patterns from the regions marked (i) and (ii). The yellow arrows in (a) are parallel to the lithium-ion diffusion path in the particle. (c) The *c*-axis lattice parameters at locations along the dashed yellow line in (a).

inhomogeneity, which leads to localized internal strain becomes increasingly severe as the Ni fraction approaches 90%.

To confirm the presence of the structural inhomogeneity within a single grain, the S-NCM90 cathode was recovered after charging to 4.3 V at 0.5 C rate, and a thin section of the charged cathode was prepared by ion beam milling and examined using transmission electron microscopy (TEM) (Figure 5a). High-resolution TEM images were obtained in a region between locations near the surface (i) and center (ii) of the S-NCM90 cathode along the direction of the lithium-ion diffusion path, as deduced from the corresponding [100] zone−axis electron diffraction patterns. To quantitatively assess the average distance between layer planes, the *c*-axis lattice parameter of each location imaged by TEM was calculated (Figure 5b and Figure S14). Figure 5c shows that the calculated *c*-axis lattice parameters tend to increase from the surface toward the center of the particle. Based on the *c*-axis lattice parameters determined from the in situ XRD result (Figure S9e), the lowest value of 13.7 Å near the surface corresponds to the highly charged state where the delithiated amount of x = ∼0.9 whereas the maximum value of 14.1 Å in the center of the particle suggests that x = ∼0.77. Consistent with the in situ XRD results in Figure 4f,h, the TEM result shows that a charged S-NCM90 cathode particle consists of regions with varying lattice parameters that developed according to the gradient profile of the lithium-ion concentration. The inhomogeneity within the cathode particle produces nonuniform spatial stress which the cathode releases by generating structural defects through planar gliding and particle fracturing during electrochemical reactions.[13,19,20,22] Such spatial inhomogeneity in the lithium-ion concentration and strain in Ni-rich S-NCM cathodes is exacerbated by repeated cycling and contributes to capacity fading in S-NCM cathodes.

In this study, a series of Ni-rich S-NCM cathodes (Ni contents of 70, 80, and 90%) with particle diameters of ∼3 μm were systematically examined to compare their characteristics and cycling behavior with those of conventional P-NCM cathodes. Unlike P-NCM cathodes susceptible to intergranular microcracking during cycling, S-NCM cathodes are resistant to mechanical fracture even at the deeply charged state or repetitive cycling. Nevertheless, the electrochemical performances of S-NCM cathodes, in terms of capacity and cycling stability, are inferior to those of P-NCM cathodes because of limited lithium-ion diffusion pathways. The difference in the electrochemical performances of S-NCM and P-NCM cathodes increases with increasing Ni fraction. The H2−H3 phase transition peaks, considered as a critical gauge of the rapid capacity fading for Ni-rich layered cathodes, faded differently with cycling, suggesting that different mechanisms govern the capacity fading of S-NCM and P-NCM cathodes. The rapid capacity fading of P-NCM cathodes is largely attributed to the formation of microcracks that allow electrolyte attack, resulting in the buildup of NiO-like rock-salt phases. In contrast, owing to the limited lithium-ion diffusion pathways of S-NCM cathodes, their lithium concentrations tend to become spatially inhomogeneous during cycling, this tendency is exacerbated by high C rates and Ni contents, resulting in the coexistence of two phases within a single cathode particle. The structural inhomogeneity at the charged S-NCM90 cathode, observed using in situ XRD and TEM, induces nonuniform stress to cause structural defects and thus limit diffusion kinetics of Li^+ ion, eventually leading to capacity fading during electrochemical reactions.

To improve the performance of LIBs, both polycrystalline and single-crystal cathodes are being investigated by academic and industrial researchers. Single-crystal cathodes have the advantages of being resistant to mechanical fracturing and tolerant of gas evolution, but deliver unsatisfactory performance, especially at high C rates. Overcoming the inhomogeneous lithium-ion and associated internal stress concentrations in S-NCM cathodes requires optimizing their particle sizes to improve lithium diffusion kinetics during operation, whereas stable, Ni-rich, fracture-resistant, P-NCM cathodes can be developed through microstructural modification.[23−25] Alternatively, a bimodal cathode featuring both S-NCM and P-NCM particles could be an effective strategy for enhancing LIB performance.

https://doi.org/10.1021/acsenergylett.1c01089
ACS Energy Lett. 2021, 6, 2726−2734

■ ASSOCIATED CONTENT

Supporting Information

The Supporting Information is available free of charge at https://pubs.acs.org/doi/10.1021/acsenergylett.1c01089.

Experimental methods, particle size analysis, SEM images and XRD patterns of lithiated oxide, rate capability test and GITT results, dQ dV^{-1} curves for various cycles, cross-sectional SEM images of cycled electrodes, in situ XRD patterns and corresponding contour plots, overlays and deconvolutions, HRTEM images, tables of particle size distribution, ICP results and of information from XRD results (PDF)

■ AUTHOR INFORMATION

Corresponding Authors

Chong S. Yoon − *Department of Materials Science and Engineering, Hanyang University, Seoul 04763, South Korea;* orcid.org/0000-0001-6164-3331; Email: csyoon@hanyang.ac.kr

Yang-Kook Sun − *Department of Energy Engineering, Hanyang University, Seoul 04763, South Korea;* orcid.org/0000-0002-0117-0170; Email: yksun@hanyang.ac.kr

Authors

Hoon-Hee Ryu − *Department of Energy Engineering, Hanyang University, Seoul 04763, South Korea*

Been Namkoong − *Department of Energy Engineering, Hanyang University, Seoul 04763, South Korea*

Jae-Hyung Kim − *Department of Energy Engineering, Hanyang University, Seoul 04763, South Korea*

Ilias Belharouak − *Electrification and Energy Infrastructure Division, Oak Ridge National Laboratory, Oak Ridge, Tennessee 37831, United States;* orcid.org/0000-0002-3985-0278

Complete contact information is available at: https://pubs.acs.org/10.1021/acsenergylett.1c01089

Author Contributions

#H.-H.R. and B.N. contributed equally to this work.

Notes

The authors declare no competing financial interest.

■ ACKNOWLEDGMENTS

This work was mainly supported by a Human Resources Development programme (No. 20184010201720) of a Korea Institute of Energy Technology Evaluation and Planning (KETEP) grant, funded by the Ministry of Trade, Industry and Energy of the Korean government. This work was also supported by National Research Foundation of Korea (NRF) grant funded by the Korea government Ministry of Education and Science Technology (MEST) (NRF-2018R1A2B3008794).

■ REFERENCES

(1) *Global Outlook 2020*; International Energy Agency: Paris, France, 2020.

(2) Myung, S.-T.; Maglia, F.; Park, K.-J.; Yoon, C. S.; Lamp, P.; Kim, S.-J.; Sun, Y.-K. Nickel-Rich Layered Cathode Materials for Automotive Lithium-Ion Batteries: Achievements and Perspectives. *ACS Energy Lett.* **2017**, *2*, 196−223.

(3) Lithium-ion battery material market 2019−major four components; Yano Research Institute, https://www.yanoresearch.com/, 2019.

(4) Noh, H.-J.; Youn, S.; Yoon, C. S.; Sun, Y.-K. Comparison of the structural and electrochemical properties of layered $Li[Ni_xCo_yMn_z]O_2$ (x = 1/3, 0.5, 0.6, 0.7, 0.8 and 0.85) cathode material for lithium-ion batteries. *J. Power Sources* **2013**, *233*, 121−130.

(5) Ryu, H.-H.; Park, K.-J.; Yoon, C. S.; Sun, Y.-K. Capacity Fading of Ni-Rich $Li[Ni_xCo_yMn_{1-x-y}]O_2$ ($0.6 \leq x \leq 0.95$) Cathodes for High-Energy-Density Lithium-Ion Batteries: Bulk or Surface Degradation? *Chem. Mater.* **2018**, *30*, 1155−1163.

(6) Li, J.; Cameron, A. R.; Li, H.; Glazier, S.; Xiong, D.; Chatzidakis, M.; Allen, J.; Botton, G. A.; Dahn, J. R. Comparison of Single Crystal and Polycrystalline $LiNi_{0.5}Mn_{0.3}Co_{0.2}O_2$ Positive Electrode Materials for High Voltage Li-Ion Cells. *J. Electrochem. Soc.* **2017**, *164*, A1534−A1544.

(7) Li, J.; Li, H.; Stone, W.; Weber, R.; Hy, S.; Dahn, J. R. Synthesis of Single $LiNi_{0.5}Mn_{0.3}Co_{0.2}O_2$ for Lithium Ion Batteries. *J. Electrochem. Soc.* **2017**, *164*, A3529−A3537.

(8) Wang, L.; Wu, B. R.; Mu, D. B.; Liu, X. J.; Peng, Y. Y.; Xu, H. L.; Liu, Q.; Gai, L.; Wu, F. Single-crystal $LiNi_{0.6}Mn_{0.2}Co_{0.2}O_2$ as high performance cathode materials for Li-ion batteries. *J. Alloys Compd.* **2016**, *674*, 360−367.

(9) Li, H.; Li, J.; Zaker, N.; Zhang, N.; Botton, G. A.; Dahn, J. R. Synthesis of Single Crystal $LiNi_{0.88}Co_{0.09}Al_{0.03}O_2$ with a Two-Step Lithiation Method. *J. Electrochem. Soc.* **2019**, *166*, A1956−A1963.

(10) Liu, Y.; Harlow, J.; Dahn, J. R. Microstructural Observation of "Single Crystal" Positive Electrode Materials Before and After Long Term Cycling by Cross-section Scanning Electron Microscopy. *J. Electrochem. Soc.* **2020**, *167*, No. 020512.

(11) Qian, G.; Zhang, Y.; Li, L.; Zhang, R.; Xu, J.; Cheng, Z.; Xie, S.; Wang, H.; Rao, Q.; He, Y.; Shen, Y.; Chen, L.; Tang, M.; Ma, Z.-F. Single-crystal nickel-rich layered-oxide battery cathode materials: synthesis, electrochemistry, and intra-granular fracture. *Energy Storage Mater.* **2020**, *27*, 140−149.

(12) Fan, X.; Hu, G.; Zhang, B.; Ou, X.; Zhang, J.; Zhao, W.; Jia, H.; Zou, L.; Li, P.; Yang, Y. Crack-free single-crystalline Ni-rich layered NCM cathode enable superior cycling performance of lithium-ion batteries. *Nano Energy* **2020**, *70*, 104450.

(13) Bi, Y.; Tao, J.; Wu, Y.; Li, L.; Xu, Y.; Hu, E.; Wu, B.; Hu, J.; Wang, C.; Zhang, J.-G.; Qi, Y.; Xiao, J. Reversible planar gliding and microcracking in a single-crystalline Ni-rich cathode. *Science* **2020**, *370*, 1313−1317.

(14) Wang, T.; Ren, K.; He, M.; Dong, W.; Xiao, W.; Pan, H.; Yang, J.; Yang, Y.; Liu, P.; Cao, Z.; Ma, X.; Wang, H. Synthesis and Manipulation of Single-Crystalline Lithium Nickel Manganese Cobalt Oxide Cathodes: A Review of Growth Mechanism. *Front. Chem.* **2020**, *8*, 747.

(15) Qian, G.; Li, Z.; Meng, D.; Liu, J.-b.; He, Y.-S.; Rao, Q.; Liu, Y.; Ma, Z.-F.; Li, L. Temperature-Swing Synthesis of Large-Size Single-Crystal $LiNi_{0.6}Mn_{0.2}Co_{0.2}O_2$ Cathode Materials. *J. Electrochem. Soc.* **2021**, *168*, No. 010534.

(16) Kim, Y. Lithium Nickel Cobalt Manganese Oxide Synthesized Using Alkali Chloride Flux: Morphology and Performance As a Cathode Material for Lithium Ion Batteries. *ACS Appl. Mater. Interfaces* **2012**, *4*, 2329−2333.

(17) Zhu, J.; Chen, G. Single-crystal based studies for correlating the properties and high-voltage performance of $Li[Ni_xMn_yCo_{1-x-y}]O_2$ cathodes. *J. Mater. Chem. A* **2019**, *7*, 5463−5474.

(18) Han, Y.; Heng, S.; Wang, Y.; Qu, Q.; Zheng, H. Anchoring Interfacial Nickel Cations on Single-Crystal $LiNi_{0.8}Co_{0.1}Mn_{0.1}O_2$ Cathode Surface via Controllable Electron Transfer. *ACS Energy Lett.* **2020**, *5*, 2421−2433.

(19) Zhang, F.; Lou, S.; Li, S.; Yu, Z.; Liu, Q.; Dai, A.; Cao, C.; Toney, M. F.; Ge, M.; Xiao, X.; Lee, W.-K.; Yao, Y.; Deng, J.; Liu, T.; Tang, Y.; Yin, G.; Lu, J.; Su, D.; Wang, J. Surface regulation enables high stability of single-crystal lithium-ion cathodes at high voltage. *Nat. Commun.* **2020**, *11*, 3050.

(20) Radin, M. D.; Alvarado, J.; Meng, Y. S.; Van der Ven, A. Role of Crystal Symmetry in the Reversibility of Stacking-Sequence Changes in Layered Intercalation Electrodes. *Nano Lett.* **2017**, *17*, 7789−7795.
(21) Khorsand Zak, A.; Abd. Majid, W.H.; Abrishami, M.E.; Yousefi, R. X-ray analysis of ZnO nanoparticles by Williamson-Hall and size-strain plot methods. *Solid State Sci.* **2011**, *13*, 251−256.
(22) Ulvestad, A.; Singer, A.; Cho, H.-M.; Clark, J. N.; Harder, R.; Maser, J.; Meng, Y. S.; Shpyrko, O. G. Single Particle Nanomechanics in Operando Batteries via Lensless Strain Mapping. *Nano Lett.* **2014**, *14*, 5123−5127.
(23) Kim, U.-H.; Park, G.-T.; Son, B.-K.; Nam, G. W.; Liu, J.; Kuo, L.-Y.; Kaghazchi, P.; Yoon, C. S.; Sun, Y.-K. Heuristic solution for achieving long-term cycle stability for Ni-rich layered cathodes at full depth of discharge. *Nat. Energy* **2020**, *5*, 860−869.
(24) Sun, H. H.; Ryu, H.-H.; Kim, U.-H.; Weeks, J. A.; Heller, A.; Sun, Y.-K.; Mullins, C. B. *ACS Energy Lett.* **2020**, *5*, 1136−1146.
(25) Ryu, H.-H.; Sun, H. H.; Myung, S.-T.; Yoon, C. S.; Sun, Y.-K. Reducing cobalt from lithium-ion batteries for the electric vehicle era. *Energy Environ. Sci.* **2021**, *14*, 844−852.

https://doi.org/10.1021/acsenergylett.1c01089
ACS Energy Lett. 2021, 6, 2726−2734